Multiscale interaction of inertial particles with turbulent motions in open channel flow

Guiquan Wang [*] and David Richter [†]
Department of Civil and Environmental Engineering and Earth Sciences, University of Notre Dame, Notre Dame, Indiana 46556, USA

(Received 6 June 2019; accepted 31 March 2020; published 27 April 2020)

Direct numerical simulations two-way coupled with inertial particles are used to investigate the particle distribution and two-way coupling mechanisms in turbulent open channel flow. In particular, the relationship between low- and high-inertia particles and the distinct large-scale motions (LSMs) and very-large-scale motions (VLSMs) which are characteristic of high-Reynolds-number, wall-bounded turbulence are examined. To do this, two methods of spatial filtering are applied to isolate the effects of LSMs versus VLSMs and separately analyze their interactions with inertial particles. One method of filtering the VLSMs from the flow is via artificial domain truncation, which alters the mean particle concentration profile and particle clustering due to the absence of VLSMs. The second method uses on-the-fly low- and high-pass filtering on the velocity field seen by the particles, so that as the simulation progresses the particles can only couple with certain scales of the flow. The results show that turbophoretic drift of particles toward the wall and the resulting increase in near-wall concentration is underpredicted without VLSMs, whereas the small-scale clustering and two-way coupling effects are mainly determined by particle coupling with LSMs. In the inner layer, the elongated streamwise anisotropic particle clustering can be reproduced by coupling solely with LSMs for low Stokes number. However, we do not observe a similar particle clustering behavior in the outer layer as seen in the full simulation by coupling particles with either LSMs or VLSMs at high Stokes numbers. This indicates that the organized particle structures are formed by the joint action of LSMs and VLSMs, especially for high-Stokes-number particles in the outer layer. The implications of these scale interactions are discussed in the context of large eddy simulation (LES) of one- and two-way coupled flows.

DOI: 10.1103/PhysRevFluids.5.044307

I. INTRODUCTION

Across a wide variety of engineered and natural systems, inertial particles are often suspended and transported by turbulent motions, and they have the potential for exchanging momentum and energy with the surrounding flow in complex ways. In particular, we are motivated by systems where the flow Reynolds number is large, allowing for multiscale interactions between individual particles and a full spectrum of turbulent motion. In the environment, this scenario occurs frequently, including sand and dust suspensions [1,2], ocean spray and aerosol generation [3], pollutants in the atmospheric boundary layer [4], cloud droplet motion and collisional growth [5], and the transport

[*]Current address: Physics of Fluids Group and Twente Max Planck Center, Department of Science and Technology, Mesa+ Institute, and J.M. Burgers Center for Fluid Dynamics, University of Twente, P.O. Box 217, 7500 AE Enschede, The Netherlands.
[†]David.Richter.26@nd.edu

of various constituents in rivers [6]. Many of these systems occur near a solid boundary, and thus canonical wall turbulence provides a favorable test bed for studying particle-turbulence interaction.

In wall turbulence, so-called large-scale motions (LSMs) play a crucial role in determining the structure and the dynamic processes of the entire inner layer [7]. The LSMs in the inner layer have characteristic lengths of $\lambda_x^+ = \mathcal{O}(1000)$ and widths of $\lambda_z^+ = \mathcal{O}(100)$ [7,8], where x and z are the streamwise and spanwise directions, respectively (the superscript "+" refers to normalization based on viscous scales, where δ_ν, u_τ, and $\tau_\nu \equiv \nu/u_\tau^2$ correspond to the viscous length scale, velocity scale, and timescale, respectively). In the outer layer, so-called very-large-scale motions (VLSMs) are observed in a variety of different wall turbulence flow configurations [9–11], and carry 40–65% of the kinetic energy and 30–50% of the Reynolds shear stress [12]. The spanwise wavelength of VLSMs scales as $\lambda_z = \mathcal{O}(h)$ while their streamwise wavelength is approximately $\lambda_x = \mathcal{O}(10h)$, where h is the boundary layer thickness in a turbulent boundary layer or half of the gap size in turbulent channel flow [9,10,13,14].

These distinct, multiscale turbulent structures result in a corresponding wide range of particle-to-fluid timescale ratios which vary as a function of wall-normal height, complicating simple descriptions of particle transport in wall turbulence [15–24]. Indeed many of these complexities exist even in wall-free shear flows [25], highlighting the need for better understanding of these phenomena. In the inner layer of wall-bounded flows, the strongly coherent ejection and sweep motions govern the particle-transfer mechanisms [18]. Conceptually, inertial particles near the wall are swept into low-speed streaks, from whence they are ejected again into the flow [26]. This in turn changes the ejection and/or sweep intensities [27], modifying near-wall turbulence nonmonotonically as a function of particle Stokes number [22]. As a result, the regeneration cycle of LSMs in the inner layer is modulated [23]. During this process, particles can be trapped within low-speed streaks for extended periods of time [18], linking this clustering process with turbophoresis [28,29]—an effect experimentally observed by Fessler *et al.* [15]. The characteristic spanwise spacing of particle clustering structures is about 100 wall units in turbulent channel flow [30], coincident with that of the spanwise LSM spacing. A large majority of the numerical work on particle-turbulence interaction in wall-bounded turbulence focuses on these inner layer dynamics.

In the outer layer, it remains computationally challenging to simulate particle-laden flow in domains which are of sufficient size to fully resolve the VLSMs, leading to a relative lack of understanding of particle coupling with outer-scale motions. Bernardini *et al.* [30] uses direct numerical simulation (DNS) to study particle clustering in VLSMs by exploiting the very-large-scale coherent motions which occur in turbulent Couette flow even at relatively low Reynolds numbers [31]. These coherent "rollers" in Couette flow [32,33] exhibit many of the same inner-outer coupling characteristics as in high-Reynolds-number boundary layers, but can be found at Reynolds numbers as low as $\mathrm{Re}_\tau = 167$ (where $\mathrm{Re}_\tau \equiv u_\tau h/\nu$ is the Reynolds number based on friction velocity u_τ, channel half-height h, and kinematic viscosity ν). In their study, Bernardini *et al.* [30] find a clear organization of particles with a spanwise spacing matching that of the very-large-scale Couette motions. However, these motions are not necessarily equivalent to the VLSMs observed in turbulent channel flow [11].

An alternative approach to studying particle-turbulence interactions with VLSMs is to perform DNS, but using a truncated domain size to save computational cost. This strategy induces artificial correlations in the streamwise direction, but this may have minimal impact on certain flow statistics [32]. Sardina *et al.* [20] studied the effect of truncating the domain size on particle distributions in turbulent channel flow and reported an increase in particle concentration at the wall of up to 20% at $\mathrm{Re}_\tau = 180$. They attributed this difference to the possible correlation of the turbulence and the near-wall particle aggregates in the truncated domain—effects which do not exist in a sufficiently large domain. As noted above, however, $\mathrm{Re}_\tau = 180$ is not high enough to separate the inner and outer regions, although weak VLSMs do still exist at this Reynolds number [34,35]. Furthermore, the recent work of Wang *et al.* [36] finds that in turbulent open channel flow up to a Reynolds number $\mathrm{Re}_\tau = 950$, truncating the domain size results in errors both in the particle concentration statistics as well as the particle velocity statistics. This discrepancy is a function of the particle Stokes number

and is largest for the Stokes numbers which cause particle accumulation in the VLSM-induced turbulent structures near the wall.

In addition to DNS, large eddy simulation (LES) can also be used with Lagrangian tracking to study high-Reynolds-number, particle-laden flows. Here, the fluid velocity at the particle position is not exactly known, but only a filtered (i.e., resolved) fluid velocity is available [37]. In particle-laden wall turbulent flow, Wang and Squires [38] show that LES predicts particle clustering reasonably well both near the wall and along the channel centerline for particles with $\mathrm{St}^+ = \mathcal{O}(10\text{–}1000)$ at $\mathrm{Re}_\tau = 180$ and 640 (where $\mathrm{St}^+ \equiv \tau_p/\tau_v$ is the Stokes number based on the particle acceleration time τ_p and the viscous wall time τ_v). For lower Stokes numbers, Marchioli *et al.* [39] find that LES of $\mathrm{St}^+ = \mathcal{O}(0.1\text{–}100)$ particles underestimates the particle wall accumulation and local segregation for $\mathrm{Re}_\tau = 180$. Fede and Simonin [40] show that particle accumulation and clustering is significantly influenced by the timescales of the unresolved subgrid motions and that it is therefore necessary to develop an accurate closure model for the interaction between inertial particles and subgrid motions in order to achieve accurate particle-laden LES (see also Jin *et al.* [41]). In the context of wall-bounded turbulence as described above, VLSMs would be resolved on an LES computational grid and could therefore influence particles directly, while LSMs would either be insufficiently or completely unresolved and would require subgrid treatment. For inertial particles, this subgrid treatment is not necessarily straightforward, since particle trajectories are the integrated result of the entire range of turbulent motions (see, for example, Pitton *et al.* [42]). It is therefore the primary goal of this study to distinguish between the role of LSMs and VLSMs, as identified via sharp cutoff filters consistent with LES formulations, on particle transport and particle-turbulence coupling, so that it is made clear which effects must be included in any future subgrid model development.

Along these lines, Wang and Richter [24] examine the effects of inertial particles on VLSMs in open channel flow using DNS at $\mathrm{Re}_\tau = 550$ and $\mathrm{Re}_\tau = 950$. They use a domain size of $L_x = 6\pi h$ and $L_z = 2\pi h$, which is comparable to the domain size used by Del Álamo and Jiménez [10] in single-phase turbulent channel flow. While not yet in an asymptotic regime [43], these Reynolds numbers are sufficiently high to produce characteristic signatures of VLSMs in the turbulent kinetic energy spectra and allow for investigating particle-turbulence coupling. Two distinct particle clustering phenomena appear in the inner layer and outer layer, corresponding to different particle Stokes numbers. One is the well-established particle clustering in near-wall streaks in the inner layer (e.g., $\mathrm{St}^+ = 24.2$), and the other is a new type of organized particle clustering structure in the outer layer (e.g., $\mathrm{St}^+ = 182$). The organized structure in the outer layer, however, is distinct from that observed in turbulent Couette flow by Bernardini *et al.* [30].

While using DNS (e.g., Wang and Richter [24]) provides insight into how particles of varying inertia influence a full range of turbulence, the nonlinearities involved make it quite challenging to differentiate between which motions, namely the LSMs and VLSMs, are responsible for the various clustering and two-way coupling features. This has obvious implications on the design of future subgrid schemes, particularly for two-way coupled flows where particles can modify the fluid. For example, perhaps it is reasonable to assume that high-Stokes-number particles simply interact with resolved motions, and therefore no subgrid treament is needed; this is the strategy of Yamamoto *et al.* [44], for example. Likewise, if low-Stokes-number particles only interact with subgrid motions, perhaps a judicious choice of subgrid velocity is sufficient (e.g., Park *et al.* [45]). As noted by Wang and Richter [24], however, a much more difficult situation may arise: Particle-turbulence interactions may occur at scales not resolved in LES, but have large impacts on VLSMs and other resolved motions. Or perhaps, since Lagrangian trajectories are the integrated effect of all scales of motion, the particle locations at the resolved scale are not correct, thereby precluding an accurate two-way coupling. This kind of upscale influence poses a serious challenge for particle-laden LES, and the current study is devoted to better elucidating the scale interactions by using multiple forms of filtering. We begin by investigating the effects of truncating the domain size, in an effort to isolate particle interactions with LSMs (i.e., exclude VLSMs). However, as discussed above, truncating the domain is not an entirely ideal method for calculating particle dynamics. Therefore, as a second method, we isolate LSMs and VLSMs and their coupling effects independently in the same turbulent flow via

spatial filtering of velocity field seen by the particles. While artificial, this technique allows us to pinpoint a set of clustering and coupling mechanisms that would, and would not, be required in a particle-laden LES subgrid model. We restrict ourselves to mass loadings of $\mathcal{O}(0.1)$, where two-way coupling effects are small but non-negligible, and expect that at higher particle concentrations, many of these nonlinearities may be enhanced due to particle collisions and other high-loading effects.

II. SIMULATION METHOD AND PARAMETERS

A. Numerical method

Direct numerical simulations of the carrier phase are performed for an incompressible Newtonian fluid. A pseudospectral method is employed in the periodic directions (streamwise x and spanwise z), and second-order finite differences are used for spatial discretization in the wall-normal (y) direction. The solution is advanced in time by a third-order Runge-Kutta scheme. Incompressibility is achieved via the solution of a pressure Poisson equation. The fluid velocity and pressure fields are a solution of the continuity and momentum balance equations in Eqs. (1) and (2), respectively:

$$\frac{\partial u_j}{\partial x_j} = 0, \tag{1}$$

$$\frac{\partial u_i}{\partial t} + u_j \frac{\partial u_i}{\partial x_j} = -\frac{1}{\rho_f}\frac{\partial p}{\partial x_i} + \nu \frac{\partial^2 u_i}{\partial x_j \partial x_j} + \frac{1}{\rho_f} F_i. \tag{2}$$

Here u_i is the fluid velocity, p is the pressure, F_i is the particle feedback force to the carrier phase computed by summing and projecting the particle force to the nearest Eulerian grid points, ν is the fluid kinematic viscosity, and ρ_f is the fluid density.

Particle trajectories and particle-laden flow dynamics are based on the point-force approximation where the particle-to-fluid density ratio $r \equiv \rho_p/\rho_f \gg 1$ and the particle size is smaller than the smallest viscous dissipation scales of the turbulence. As a consequence of this and the low volume concentrations (a maximum bulk volume fraction of Φ_V less than 1×10^{-3}), only the Schiller-Naumann [46] hydrodynamic drag force is considered. The velocity of particle n is governed by Eq. (3) and particle trajectories are then obtained from numerical integration of the equation of motion in Eq. (4):

$$\frac{du^n_{p,i}}{dt} = f^n_i, \tag{3}$$

$$\frac{dx^n_i}{dt} = u^n_{p,i}, \tag{4}$$

where the drag is given by

$$f^n_i = \frac{1}{\tau_p}\left[1 + 0.15\left(\mathrm{Re}^n_p\right)^{0.687}\right]\left(u^n_{f,i} - u^n_{p,i}\right). \tag{5}$$

Here, $\tau_p = \rho_p {d_p}^2/(18\rho_f \nu)$ is the Stokes relaxation time of the particle, and the particle Reynolds number $\mathrm{Re}^n_p = |u^n_{f,i} - u^n_{p,i}| d^n_p/\nu$ is based on the magnitude of the particle slip velocity $(u^n_{f,i} - u^n_{p,i})$ and particle diameter d^n_p. In this work, the average Re^n_p is less than 1.0, which is far smaller than the suggested maximum $\mathrm{Re}_p \approx 800$ for the Stokes drag correction in Eq. (3). As a result of the low Re_p, the correction to the Stokes drag is minimal in this study. Other terms in the particle momentum equation are neglected since they remain small compared with drag when the density ratio $r \gg 1$ [47]. In all simulations, particles are initially distributed at random locations throughout the channel. Particle-particle collisions are not taken into consideration, and we exert a purely elastic collision between particles and the lower wall and the free surface of the open channel flow. Gravity is not included so as to focus specifically on the role of turbulence in particle transport.

Since the projection method of treating the coupling of point particles can in certain cases be grid dependent, other techniques have been developed which can be used to account for two-way

TABLE I. Parameters of numerical simulations.

Type 1 large domain

$$N_x \times N_y \times N_z = 1024 \times 128 \times 512$$
$$L_x \times L_y \times L_z = 6\pi \times 1 \times 2\pi$$
$$L_x^+ \times L_y^+ \times L_z^+ = 10367 \times 550 \times 3456$$
$$\Delta x^+ \times \Delta y^+(\text{wall, surface}) \times \Delta z^+ = 10.1 \times (1,\ 7.2) \times 6.75$$

Type 2 small domain

$$N_x \times N_y \times N_z = 128 \times 128 \times 128$$
$$L_x \times L_y \times L_z = 2.5 \times 1 \times 1.5$$
$$L_x^+ \times L_y^+ \times L_z^+ = 1375 \times 550 \times 825$$
$$\Delta x^+ \times \Delta y^+(\text{wall, surface}) \times \Delta z^+ = 10.7 \times (1,\ 7.2) \times 6.45$$

Type	Num	Φ_m	ρ_p/ρ_f	Φ_v	N_p	τ_p	St^+	St_{LSM}	St_{VLSM}
1	case0				Unladen flow				
2	case0_{small}				Unladen flow				
1	case1	0.14	160	8.75×10^{-4}	7.33×10^6	5.1	24.2	0.3025	0.044
1	case1_{LSM}				7.33×10^6				
1	case1_{VLSM}				7.33×10^6				
2	case1_{small}				2.32×10^5				
1	case2	0.14	1200	1.17×10^{-4}	9.8×10^5	38.2	182	2.275	0.331
1	case2_{LSM}				9.8×10^5				
1	case2_{VLSM}				9.8×10^5				
2	case2_{small}				3.1×10^4				

coupling in particle-laden flows. For example, Capecelatro and Desjardins [48] use a volume filtering operator to replace the point sources by smoother, locally filtered fields. Recently, Sardina *et al.* [49] use a similar scheme to calculate the back-reaction term for small bubbles. In efforts to account for far-field disturbances from the particle on the interpolated field, Gualtieri *et al.* [50] present an exact regularized point particle method which applies a Stokeslet approximation. Akiki *et al.* [51] introduce an pairwise interaction extended point-particle model which attempts to account for the microscale flow induced by the neighboring spheres by making use of their precise location. It is the goal of all of these techniques to attempt to mimic finite-size particles and fully resolved simulations with an acceptable computational cost, particularly when local particle concentrations are large. For the current model, we validate our implementation of the point particle method in Wang *et al.* [52], where comparisons against the code of Capecelatro and Desjardins [48] and the experiments of Fong *et al.* [53] show that for the volume fractions and particle Stokes numbers used herein, the errors incurred from our method of two-way coupling are small.

B. Numerical parameters and domain setup

The flow configuration of interest is pressure-driven open channel flow (note that by "open channel" we refer to the boundary conditions of our setup and do not imply that this is a solid-liquid flow; indeed the density ratio used is characteristic of gas-solid flows). A no-slip condition is imposed on the bottom wall and a shear-free condition is imposed on the upper surface; such boundary conditions have been proven capable of capturing many of the phenomena (e.g., VLSMs) seen in experiments with shear-free upper boundaries—see Refs. [14,16,54]. Grid independence and single-phase flow validation against Yamamoto *et al.* [55] at $\text{Re}_\tau = 200$ can be found in Wang and Richter [24].

An overview of the simulation cases is presented in Table I. The friction Reynolds number is $\text{Re}_\tau \equiv u_\tau h/\nu = 550$, where h is the depth of the open channel. In particle-laden flow, the time

evolution of the flow Reynolds number is monitored during the simulation and we find that the two-way coupling has a negligible effect (less than 1%) in modifying the Reynolds number with the current mass loading. The "large domain" has been demonstrated to fully capture VLSMs in the outer layer, and the streamwise turbulent kinetic energy spectrum is nearly unchanged compared with a doubled domain size [24].

In the inner layer ($y^+ < 100$), an autonomous regeneration mechanism maintains near-wall turbulence (above $y^+ \approx 20$), where the characteristic scale of LSMs is roughly $L_y^{LSM,+} \approx 80$. Wang *et al.* [56] define a characteristic timescale $\tau_f^{LSM,+} = L_y^{LSM,+}/\max(v'^+_{rms}|w'^+_{rms})$ (where subscript "rms" refers to the root-mean-square and the max takes the larger of the spanwise or wall-normal rms velocity fluctuation), which is related to the LSMs and is approximately equal to 80. In the outer layer, the VLSMs nearly extend from the bottom wall to the upper free surface, where their characteristic length scale is found to be $L_y^{VLSM,+} \approx 550$. We similarly define a characteristic timescale $\tau_f^{VLSM,+} = L_y^{VLSM,^+}/\max(v'^+_{rms}|w'^+_{rms})$ specific to VLSMs, which is approximately 550. From these, two Stokes numbers are defined for each particle, denoted by $\mathrm{St}_{LSM} \equiv \mathrm{St}^+/\tau_f^{LSM,+}$ and $\mathrm{St}_{VLSM} \equiv \mathrm{St}^+/\tau_f^{VLSM,+}$. The ratio d_p/η_K is maintained at a value of approximately 0.42, where η_K is the Kolmogorov length, and the particle Reynolds number remains $\mathcal{O}(1)$ or lower. Φ_m is the bulk particle mass concentration in the domain, and N_p is the total particle number.

As stated above, the overarching goal of this work is to use spatial filtering to untangle the scale dependence of particle-turbulence interactions, particularly when LSMs and VLSMs coexist in the turbulent flow. In our former work [24], low-Stokes-number particles of $\mathrm{St}^+ = 24.2$ ($\mathrm{St}_{LSM} = 0.3025$) are more preferentially located within low-speed regions in the inner layer, whereas high-Stokes-number particles of $\mathrm{St}^+ = 182$ ($\mathrm{St}_{VLSM} = 0.331$) tend to form distinct clustering structures in the outer layer. Furthermore, Wang *et al.* [36] systematically study the effect of domain size on particle one-point statistics for St^+ ranging from 2.42 to 908 at $\mathrm{Re}_\tau = 550$ and 950, and they find that the domain size has the strongest effect on particles of $\mathrm{St}^+ = \mathcal{O}(10)$, but little effect on particles of $\mathrm{St}^+ = \mathcal{O}(100)$. Based on these distinct dynamics, we choose these two particular Stokes numbers for the current study, corresponding to case1 and case2 in Table I, since they exhibit a preferential response to the timescales associated with LSMs and VLSMs, respectively.

Two approaches are used to artificially filter the effects of certain spatial scales from the particle-turbulence coupling. The first is by simply using domain truncation to effectively remove VLSMs from the flow by restricting the size necessary to sustain them. These simulations are referred to as "small" in Table I. The truncated cases are used to contrast the particle dynamics in flows with nominally the same Reynolds number but with differences in the nature of the coherent structures—i.e., LSMs and their regeneration are captured on the small grids, while VLSMs are not. These results are presented in Sec. III A. The second method uses the large domain size (sufficient size to capture VLSMs) but applies spatial filtering to the velocity field seen by the particles. Here, we use a low-pass filter for examining particle interactions with only VLSMs and a high-pass filter for isolating interactions with LSMs, in order to isolate individual scale couplings and further investigate the mechanism of small-scale particles affecting large-scale motions (a challenge for LES subgrid model development) [23]. These results are presented in Sec. III B. It should be emphasized that we do not claim that these filtering scenarios are somehow representations of specific physical systems; rather, they are tools for decoupling and better understanding the nonlinearities which exist when particles interact with a full range of turbulent motion. We also note that this artificial filtering technique, while providing key insights into the multiscale particle-turbulence interaction problem, necessarily leaves some questions unanswered. For example, other strategies would need to be used to better distinguish scale effects on Lagrangian trajectories, since our filtering operators modify the locations of the particles relative to where they would have been otherwise. As stated above, our goal is to focus specifically on the role of scale filtering (i.e., that associated with LES) and how one- and two-way coupling responds in this context; further work would be required to complete the picture.

III. RESULTS

A. Filtering by domain truncation

The distribution and transport of inertial particles are determined by the multiscale turbulent structures in wall turbulence, especially at Reynolds numbers which support multiple decades of spatial and/or temporal scale separation. For unladen wall-bounded turbulence, several studies have sought to quantify the effects of domain size [57–59], and in particular identify the minimum domain extent which still captures accurate one-point statistics while avoiding the effects of periodic boundary conditions in the streamwise or spanwise directions. These efforts have obvious implications for minimizing computational costs while performing DNS of high-Reynolds-number turbulent flows.

In the viscous and buffer layers, Jiménez and Moin [60] identify a minimal box with size $L_x^+ =$ 300–600 and $L_z^+ =$ 80–160 which is able to isolate the wall-attached structures. The low-order turbulence statistics are in good agreement with experiments in the near-wall region, which is due to the fact that VLSMs carry little Reynolds stress near the wall in full-spectrum turbulence and are largely independent from the autonomous LSMs [61]. In an effort to understand near-wall turbulence maintenance and transition, Hamilton *et al.* [62] use the smallest possible domain to study the regeneration cycle of LSMs in the inner layer at low Reynolds numbers.

In the logarithmic and outer regions, Flores and Jiménez [57] show that similar minimal domains exist for the logarithmic and outer layers of turbulent channels, but that size ($L_x = 6h$ and $L_z = 3h$) is much larger than in the work of Jiménez and Moin [60]. Similarly, Lozano-Durán and Jiménez [59] demonstrate that a domain size of $L_x = 2\pi h$ and $L_z = \pi h$ is sufficiently large to reproduce the one-point statistics of larger boxes at $\mathrm{Re}_\tau =$ 547–4050, and Hwang and Cossu [58] show that the self-sustaining nature of VLSMs is maintained only if the streamwise and spanwise box sizes are larger than the minimal values $L_x = 3h$ and $L_z = 1.5h$ at $\mathrm{Re}_\tau = 550$.

Meanwhile in particle-laden flow, Sardina *et al.* [20] compare domain sizes of $[L_x, L_z] = [4\pi h, 4\pi/3h]$ ($[L_x^+, L_z^+] = [2260, 754]$) with $[L_x, L_z] = [12\pi h, 4\pi h]$ in a turbulent channel at $\mathrm{Re}_\tau = 180$. The smaller of these two domain sizes is larger than the minima suggested by Hwang and Cossu [58] and Lozano-Durán and Jiménez [59], indicating that both capture any effects of VLSMs in the outer layer, mixing the effects of LSMs and VLSMs on particle transport (although the VLSMs, if even present, are very weak at such a low Reynolds number). At higher Reynolds numbers Wang *et al.* [36] show that domain truncation alters the process of turbophoresis and can modify one-point particle statistics, including concentration. In the following, we exploit these truncation effects to contrast particle interactions with LSMs alone versus the full range of turbulence.

1. Unladen energy spectrum

For the truncated simulations, we choose a domain size of $[L_x, L_z] = [2.5h, 1.5h]$ to exclude the VLSMs in the outer layer [58], corresponding to $[L_x^+, L_z^+] = [1375, 825]$ in wall viscous units. The streamwise extent is not sufficiently long to exclude the correlation of LSMs in the inner layer. The premultiplied, two-dimensional energy spectrum of streamwise velocity, $k_x k_z \Phi_{u'u'}$, where $\Phi_{u'u'} = \langle \hat{u}'(k_x, k_z, y) \hat{u}'^*(k_x, k_z, y) \rangle$, is shown in Fig. 1 for $\mathrm{Re}_\tau = 550$ for the unladen case. Here, $\hat{u}'$ is the Fourier coefficient of u', k_x is the streamwise wave number, and k_z is the spanwise wave number (λ_x and λ_z are the corresponding streamwise and spanwise wavelengths). In Fig. 1(a), we can qualitatively see that the small domain ($\mathrm{case0}_{small}$) generally captures the turbulent structures in the inner layer ($y^+ < 100$). However, the VLSMs in the inner and outer layers are completely lacking in the small domain simulation, by design.

Cross sections of the spectra at $y^+ = 15$ and $y^+ = 273$ are compared between case0 and $\mathrm{case0}_{small}$ in Figs. 1(b) and 1(c), respectively. In both of these figures, results from the DNS of Del Álamo and Jiménez [10] are also included as a reference, since these come from turbulent channel flow at the same Re_τ and should therefore have a similar spectrum. The contour of $k_x k_z \Phi_{u'u'}$ for

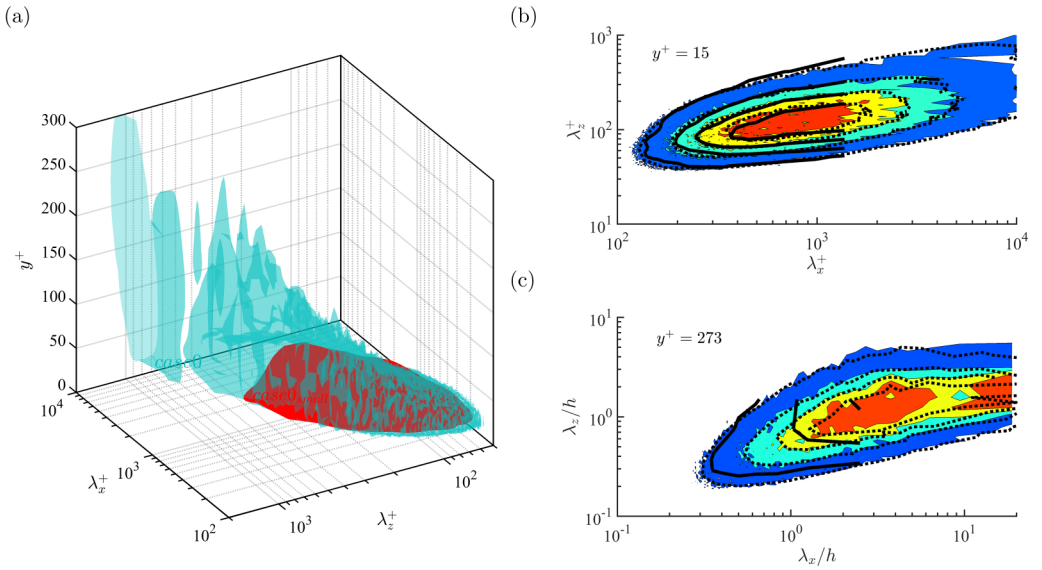

FIG. 1. Premultiplied two-dimensional energy spectrum $k_x k_z \Phi_{u'u'}/u_\tau^2$ as a function of λ_x and λ_z for case0 and case0$_{small}$. (a) In the wall-normal direction y, isosurface of 0.1 times the maximum value of the unladen flow is illustrated. Aqua is case0 and red is case0$_{small}$. Panels (b) and (c) refer to $y^+ = 15$ and $y^+ = 273$, respectively. In panels (b) and (c), the filled contours represent the large domain, lines are from the small domain, and dotted lines are from the work of Del Álamo and Jiménez [10].

the large domain agrees well with the results from Del Álamo and Jiménez [10]. In the inner layer, the energetic LSMs in case0$_{small}$ are nearly the same as in case0, whereas the tail of the spectrum [i.e., $\lambda_x > 5h$ in Fig. 1(c)] represents the deep u modes [10] or VLSM footprints [11], which are imposed by VLSMs from the outer layer and therefore are absent in case0$_{small}$. In the outer layer, the premultiplied two-dimensional energy spectrum of case0$_{small}$ is significantly different from case0, which indicates that VLSMs are not captured in the smaller domain simulation, as expected.

As another means of quantifying the scales of motion in the unladen simulations, the spanwise wavelengths $\lambda_{z,max}$ of the most energetic structures obtained from the one-dimensional (1-D) premultiplied energy spectra of u' for case0 and case0$_{small}$ are shown in Fig. 2. Results of Abe

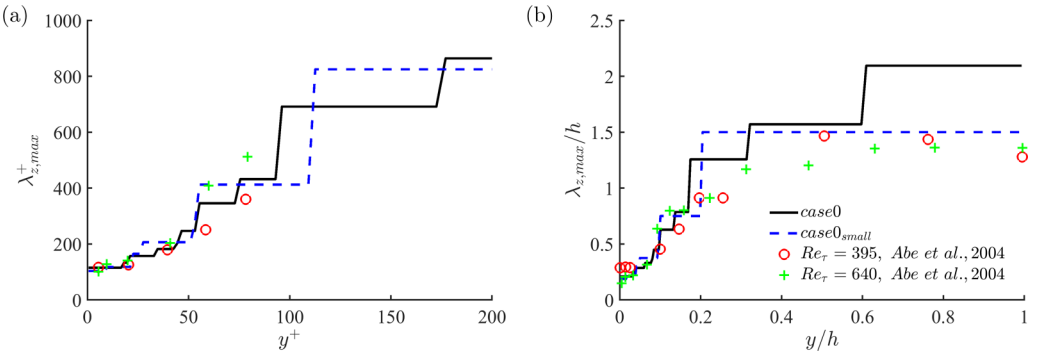

FIG. 2. Spanwise wavelengths of the most energetic structures obtained from the premultiplied energy spectra of u' for case0 and case0$_{small}$ at $\mathrm{Re}_\tau = 550$ compared with results of Abe *et al.* [63] at $\mathrm{Re}_\tau = 395$ and 640 in channel flow. (a) Wall units; (b) in outer units.

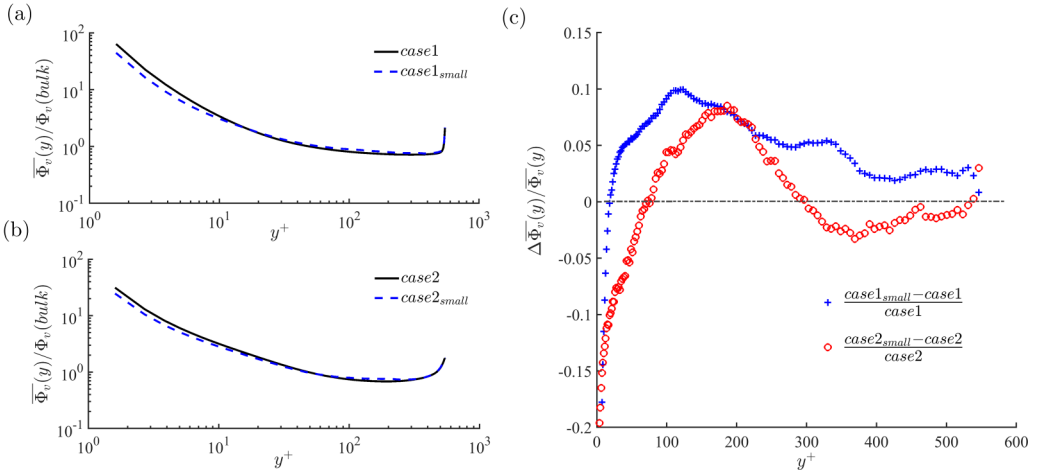

FIG. 3. Mean particle volume concentration $\overline{\Phi_v}$ as a function of wall-normal direction, scaled by Φ_v. (a) Low Stokes number, comparison between case1$_{small}$ and case1; (b) high Stokes number, comparison between case2$_{small}$ and case2. (c) The difference between the small and large domains, normalized by the results of large domain simulation.

et al. [63] at $\mathrm{Re}_\tau = 395$ and 640 in turbulent channel flow are plotted as well for comparison, since their domain sizes are sufficiently large for capturing VLSMs ($[L_x, L_z] = [12.8h, 6.4h]$). In general, the scale of $\lambda_{z,max}$ increases with wall-normal height and the scale of $\lambda_{z,max}$ in open channel flow is wider than it is in channel flow [63]. In the inner layer, where turbulent channel flow and open channel flow are expected to exhibit similar statistics, the energetic structures indeed have very similar sizes, even for the truncated domain. In the outer layer, however, we see that the primary effect of truncating the domain is to limit the spanwise wavelength of the most energetic structures, which actually become similar to turbulent channel flow at the same Reynolds number [63]. It is this difference in the outer layer, which will allow us to probe the influence of VLSMs on particle transport.

2. Particle distribution

We now turn our attention to the particle distributions in the large and small domains, with emphasis on the effect of truncating the VLSM signatures in the small domain. Mean particle volume concentrations compared between the domain sizes are shown in Fig. 3. For both low- and high-Stokes-number particles in Figs. 3(a) and 3(b), respectively, there are fewer particles in the near-wall region of the small domain simulation compared to the large domain simulation, while the opposite trend is observed in the outer region. This is the same behavior found at $\mathrm{Re}_\tau = 180$ [20] and $\mathrm{Re}_\tau = 950$ [36] with similar particle Stokes numbers based on the inner viscous timescale. The relative difference of mean particle volume concentration is shown in Fig. 3(c). With a truncated domain, a decrease of up to 20% is found near the wall compared to the large domain. This suggests that the turbophoretic effect is enhanced in the large domain simulation, owing to the presence of VLSMs in the outer layer. On the other hand, much of the bulk of the domain sees a larger concentration of the small domain as compared to the large domain. Low-Stokes-number particles (case1) see a larger concentration at all points $y^+ \gtrsim 15$, while large-Stokes-number particles (case2) have a relative concentration which alternates between positive and negative with increasing wall-normal distance. This is a result of high-inertia particles ($\mathrm{St}_{VLSM} = 0.331$ of case2) preferably responding to VLSMs in the large domain as compared to the low-inertia particles ($\mathrm{St}_{VLSM} = 0.044$ in case1). The observed differences due to the truncated domain size effect are consistent with those

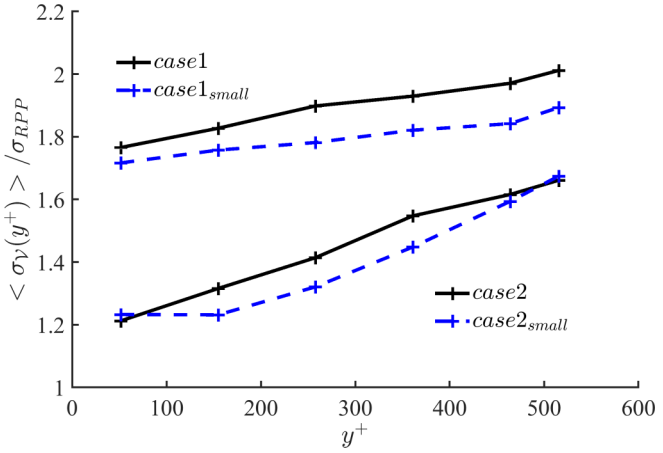

FIG. 4. Standard deviation of the normalized Voronoï area $\sigma_{\mathcal{V}}$, normalized by that of a random Poisson process, σ_{RPP}, as a function of height in wall-normal direction of low and high Stokes numbers in small domain and large domain.

observed by Sardina *et al.* [20], despite the Reynolds number and thus the effects of VLSMs being significantly larger in the present work.

As proposed by Monchaux *et al.* [64,65], a Voronoï diagram can be used to identify and quantify particle clusters and voids. The standard deviation of the distribution of Voronoï areas is directly linked to the level of clustering. For the present study, the instantaneous particle locations are analyzed in six slabs with thicknesses of $2d_p$ at multiple wall-normal distances. Figure 4 displays the standard deviation ($\sigma_{\mathcal{V}}$) of the distribution of the normalized Voronoï area $\mathcal{V} = A/\overline{A}$, where the inverse of the average Voronoï area $\overline{A}$ indicates the mean particle concentration. $\sigma_{\mathcal{V}}$ is scaled by the standard deviation of a random Poisson process (RPP; $\sigma_{RPP} = 0.52$), which would be expected if particles were randomly distributed. The ratio $\sigma_{\mathcal{V}}/\sigma_{RPP}$ exceeding unity indicates that particles are accumulating in clusters as compared to truly randomly distributed particles.

From Fig. 4, it is observed that in the inner layer ($y^+ = 50$) there are only small differences in the accumulation tendencies between the small and large domains. This is true for both Stokes numbers, indicating that clustering in this region is not directly affected by the presence of VLSMs in the outer layer. Away from the wall ($150 \leqslant y^+ \leqslant 457$), the particle clustering effect is stronger in the large domain simulation than it is in the small domain simulation, and this is true for both Stokes numbers. Near the free surface, the particle clustering is nearly the same for the high Stokes number particles, whereas the low-inertia particles see more preferential accumulation in the larger domain.

Based on the analysis of the mean particle distribution and the clustering behavior, it is evident that in the inner layer, the particle concentration increases up to 20% due to the combined influence of VLSMs and LSMs. In the outer layer, particles tend to form strong clusters due to the influence of VLSMs, and this aids the turbophoretic drift of inertial particles toward the lower wall. Thus, even while particle clustering behavior at the wall is independent of VLSMs (cf. Fig. 4), modification to the turbulent structures in the outer layer and the resulting change in particle clustering weakens the mean concentration at the wall.

B. Filtering of velocity seen by particles

As discussed in the previous section, the removal of VLSMs by domain truncation modifies the bulk transport of particles. As in other studies [20,36], it is seen that mean particle concentrations are altered when the VLSM structures are absent and that clustering characteristics are modified

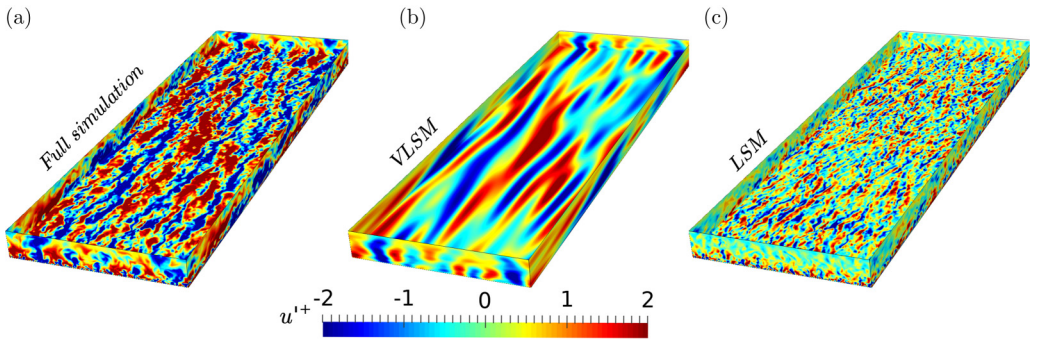

FIG. 5. Instantaneous contours of streamwise velocity fluctuation on a wall-parallel plane at $y^+ = 100$ (and domain boundary walls) in single-phase flow (case0), normalized by u_τ. (a) Full simulation containing all modes; (b) the same flow field but only associated with VLSMs, containing modes with $\lambda_x > 5h$, $\lambda_z > 0.75h$; and (c) the same flow field but only associated with LSMs, containing modes with $\lambda_x < 5h$, $\lambda_z < 0.75h$.

as well. Despite this, however, removing VLSMs by shrinking the computational domain does not fully address the scale interaction question posed in the introduction. To better untangle the nonlinear interactions between particles of very different Stokes number (i.e., case1 and case2) and disparate turbulent structures (LSMs and VLSMs), in this section we retain the large domain size, but via spatial filtering only allow particles to couple with specific scales of the turbulent flow. As noted above, this is a purely artificial process for isolating different scale interactions (i.e., not meant to represent a physical system), but will aid in future development of LES subgrid models by highlighting how small-scale particle-turbulence coupling influences large-scale motions.

1. Filtered fluid velocity

The filtered fluid velocity fields used for isolating LSMs and VLSMs (only used to couple with particles), $\widetilde{\mathbf{u}}$, are computed as

$$\widetilde{\mathbf{u}}(x, y, z, t) = \mathcal{F}^{-1} \begin{cases} \hat{\mathbf{u}}(\lambda_x, y, \lambda_z, t), & \text{if } [\lambda_x, \lambda_z] \in \text{ LSMs or VLSMs} \\ 0 & \text{otherwise,} \end{cases} \tag{6}$$

where $\mathcal{F}^{-1}$ is the inverse Fourier transform, and $\hat{\mathbf{u}}(\lambda_x, y, \lambda_z, t)$ is the 2-D Fourier transform of the fluid velocity $\mathbf{u}(x, y, z, t)$ in the two homogeneous (x and z) directions at every plane in the wall-normal direction at every time step. We define the length scale of the LSMs as $\lambda_x < 5h$, $\lambda_z < 0.75h$ and that for VLSMs as $\lambda_x > 5h$, $\lambda_z > 0.75h$, in accordance with that used by Del Álamo and Jiménez [10]. In the sections below, the cases will be referred to as case1, 2_{LSM} and case1, 2_{VLSM} when particles are coupled with LSMs or VLSMs, respectively (as denoted in Table I).

The instantaneous streamwise velocity fluctuation (u') on a wall-parallel plane at $y^+ = 100$ (and sidewalls) is shown in Fig. 5(a), and the corresponding spectral information and turbulent kinetic energy can be found in Wang and Richter [24]. Clearly, the multiscale and turbulent field is composed of both large-scale and very-large-scale motions. By applying Eq. (6), the instantaneous velocity fields containing only LSMs or VLSMs can be retrieved from the full simulation at any time step as shown in Figs. 5(b) and 5(c), respectively. The elongated, streamwise VLSMs are characterized by alternating low-speed and high-speed regions in the spanwise direction, extending from the bottom wall to the free surface in the wall-normal direction [Fig. 5(b)]. The LSMs are also elongated in the steamwise direction with alternating low-speed and high-speed regions [Fig. 5(c)], similar to the VLSMs, but at a much shorter spatial scale and only near the lower wall. It is evident from Fig. 5 that the domain size captures the many streamwise extents of LSMs, while some degree of correlation appears to occur for VLSMs in the streamwise direction. This has been tested on

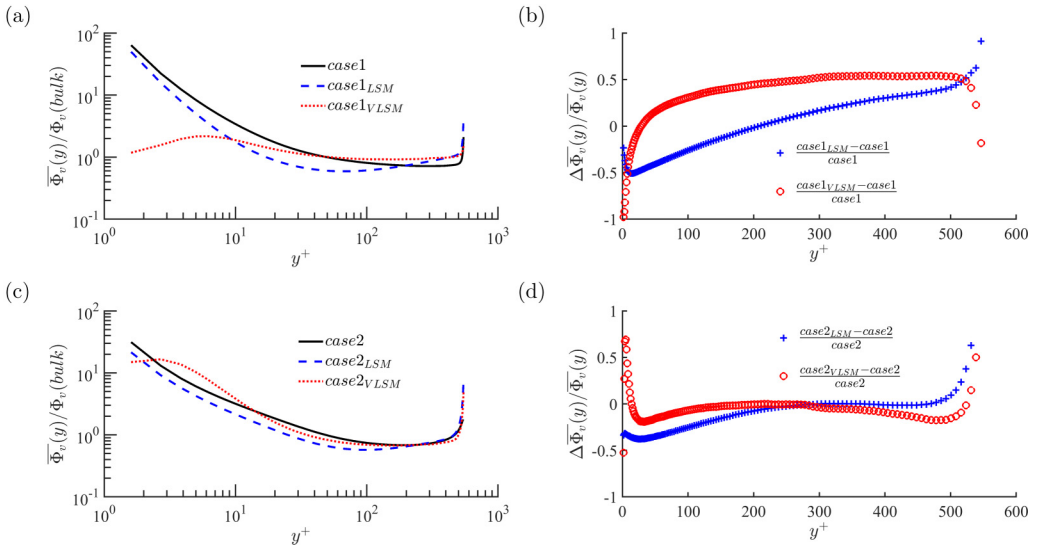

FIG. 6. Mean particle volume concentration in wall-normal direction, compared between the full and filtered velocity fields, scaled by Φ_v. [(a), (b)] Low Stokes number, comparison of case1, case1_{LSM}, and case1_{VLSM}. [(c), (d)] High Stokes number, comparison of case2, case2_{LSM}, and case2_{VLSM}. [(b), (d)] The relative difference between the filtered concentrations and the full simulation, normalized by the results of the full simulation.

larger domains [36], and the turbulence and particle statistics associated with VLSMs are virtually unchanged with larger domains.

Therefore, at every Runge-Kutta substep, a new full-spectrum velocity field is produced by the Eulerian solver, a copy of this field is then filtered based on Eq. (6), and inertial particles are only allowed to interact with this filtered flow field $\widetilde{\mathbf{u}}$. Bulk momentum conservation is still maintained, and the particle feedback forces are computed based on their interaction with the filtered field.

2. Particle distribution

The mean volume concentrations of particles coupled to the filtered velocity fields are compared to the full simulation in Fig. 6—for low Stokes number in Figs. 6(a) and 6(b) and for high Stokes number in Figs. 6(c) and 6(d). For both low- and high-inertia particles coupled to LSMs (case1, 2_{LSM}), the wall-normal particle concentration profile has a similar shape compared to the full simulations (case1, 2). Quantitatively, compared with the full simulations, *case*1_{LSM} and case2_{LSM} underpredict (less than ≈50%) the particle concentration in the region of $y^+ \leqslant 200$, whereas case1_{LSM} and case2_{LSM} overpredict (less than ≈50%) the particle concentration in the region of $y^+ \geqslant 200$. The trend is similar to that observed in the truncated domain as discussed in Sec. III A 2. From this, we confirm that the particle concentration and the effects of turbophoresis are truly underpredicted throughout much of the domain when VLSMs are absent.

Particle transport behavior by VLSMs, however, is distinctly different for both the low- and high-inertia particles as compared with the full simulations. For low-inertia particles as shown in Figs. 6(a) and 6(b), the particle wall-normal concentration profile of case1_{VLSM} is flatter than it is in the full simulation. This is due to the fact that compared to the timescale of the outer-scale motions, the low-inertia particles effectively act as tracers and thus do not exhibit any turbophoretic drift. At the same time, the particles do not feel the small-scale motions at the wall since they are filtered out, and thus the profile remains flatter there as well. Quantitatively, case1_{VLSM} seriously underpredicts (exceeding 100% in magnitude) the particle concentration in the near-wall region of

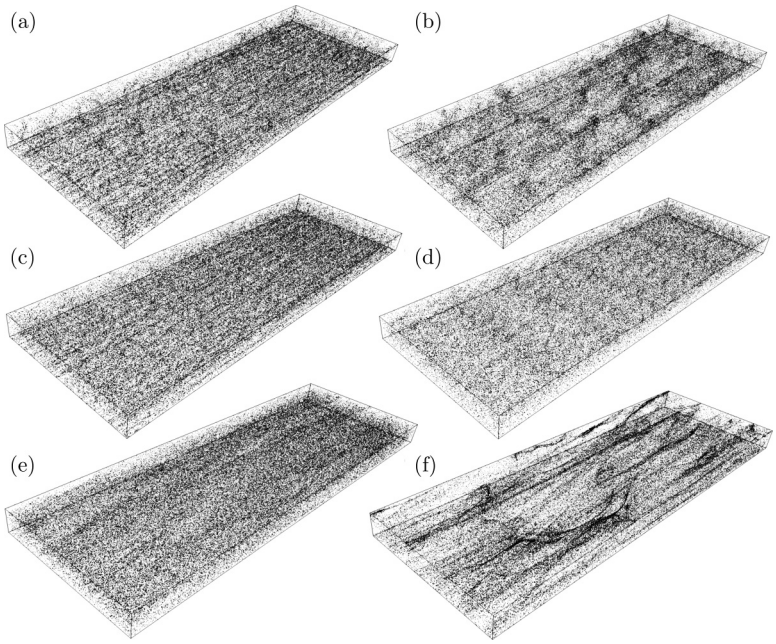

FIG. 7. Instantaneous snapshots of particle locations (black dots). [(a), (c), (e)] Low-Stokes-number particles; [(b), (d), (f)] high-Stokes-number particles. (a) case1; (b) case2; (c) case1_{LSM}; (d) case2_{LSM}; (e) case1_{VLSM}; (f) case2_{VLSM}.

$y^+ \leqslant 40$, whereas it overpredicts (less than 50% in magnitude) the particle concentration in the region of $y^+ \geqslant 40$.

For high-inertia particles, as shown in Figs. 6(c) and 6(d), the shape of the particle concentration profile of case2_{VLSM} is generally similar to that of the full simulation except very close to the wall ($y^+ \leqslant 3$). In this near-wall region, case2_{VLSM} overpredicts the particle concentration ($3 \leqslant y^+ \leqslant 13$) by upward of 50%. Elsewhere in the domain ($13 \leqslant y^+ \leqslant 530$), the particle concentration profile agrees fairly well with the full simulation. The relatively minor differences between case2 and case2_{VLSM} throughout the bulk of the domain suggest that the transport of high-inertia particles are largely due to the dynamics of the VLSMs, except very close to the boundaries. This is consistent with the idea that these larger particles would act ballistically with regards to the LSMs. For the low-inertia particles, it is clear that LSMs play a critical role in distributing the particles throughout the domain [case1_{VLSM} in Fig. 6(a)], but it is also evident that VLSMs play a role as well [case1_{LSM} underpredicting in the range $10 < y^+ < 100$ in Fig. 6(a)].

Figure 7 presents instantaneous snapshots of particle locations (black dots) for the cases under consideration. Compared to Fig. 7(a) for the full simulation (case1), we observe in Fig. 7(e) that particles distribute more randomly when they only couple with VLSMs (case1_{VLSM}) for low Stokes number. When coupled to LSMs, the particles qualitatively exhibit the particle streaks close to the wall [Fig. 7(c); these trends will be confirmed statistically below]. The particle response to LSMs and VLSMs is significantly different for high-inertia particles compared with low-inertia particles. Figure 7(b) shows that for the full simulation laden with high-inertia particles (case2), there are two distinct clustering structures: the streamwise elongated particle streaks in the inner layer and 3-D "blobs" of particles in the outer layer. Particles coupled with the LSMs [case2_{LSM} in Fig. 7(d)] form smaller scale clusters which have both a spanwise and a streamwise periodicity, while particles coupled with the VLSMs [case2_{VLSM} in Fig. 7(f)] form elongated, anisotropic structures in the outer layer which differ in shape and strength from those in the fully coupled simulation. In addition,

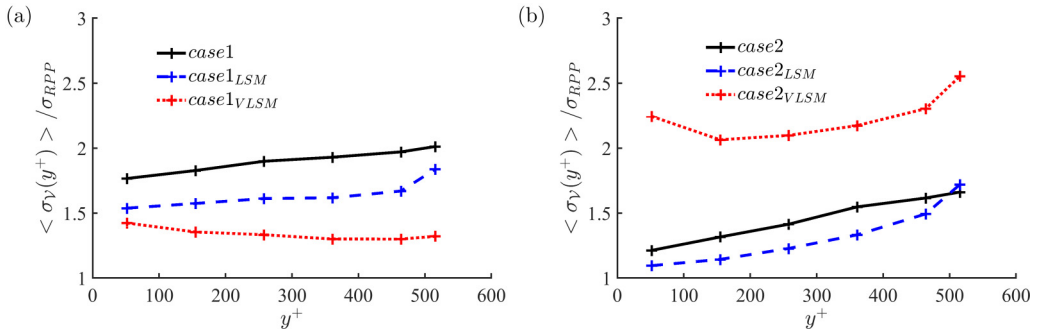

FIG. 8. Standard deviation of the normalized Voronoï area $\sigma_{\mathcal{V}}$, normalized by that of a random Poisson process, σ_{RPP}, as a function of height in wall-normal direction for (a) low and (b) high Stokes numbers coupled with different turbulent structures: full simulation (case1, 2), LSMs (case1, 2_{LSM}), and VLSMs (case1, 2_{VLSM}).

Fig. 7 highlights a challenge associated with multiscale particle-turbulence interaction: When only responding to filtered velocity fields, the particles themselves collect in different regions than they would have otherwise. Even in the one-way coupled regime, LES subgrid model development would need to ensure that the influence of unresolved motions on particle trajectories is accurately represented; the effects on two-way coupling are therefore compounded and conflated.

In order to better quantify the particle clustering behavior shown in Fig. 7, we again employ a Voronoï diagram analysis, shown in Fig. 8. For the low-inertia particles in Fig. 8(a), the ratio $\sigma_{\mathcal{V}}/\sigma_{RPP}$ is highest in the full simulation (case1) but lowest when particles are coupled only with VLSMs. In addition, $\sigma_{\mathcal{V}}/\sigma_{RPP}$ increases monotonically with increasing wall-normal distance in case1 and case1_{LSM}, while it decreases slightly in case1_{VLSM}, indicating a weak clustering when the particle/VLSM response timescale ratio ($\mathrm{St}_{VLSM} = 0.044$) is small. As noted above, the low-inertia particles effectively act as tracers with respect to the VLSM structures. For the high-inertia particles in Fig. 8(b), the ratio $\sigma_{\mathcal{V}}/\sigma_{RPP}$ is slightly smaller in case2_{LSM} than it is in the full simulation (case2). However, it is far larger in case2_{VLSM} than it is in case2 due to the strong, elongated features which form in case2_{VLSM} and are seen clearly in Fig. 7(f). The high-inertia particles clearly respond preferentially to the timescales of the VLSMs in the outer layer and thus form streaks qualitatively similar to the VLSM structures seen in Fig. 5(b).

To gain further insight into the anisotropic character of the particle clustering, the two-dimensional angular distribution functions (ADF) are calculated as defined in Eq. (7), where particles are taken from a slab with thickness of $2d_p$:

$$\mathrm{ADF}(r,\theta) = \frac{\sum_{i=1}^{n_p} \delta N_i(r,\theta)/(\delta r \delta\theta n_p)}{N/(L_x L_y)}, \quad 0 \leqslant \theta \leqslant \pi/2, \tag{7}$$

where $\delta N_i(r)$ is the particle number between $r - \delta r/2$ and $r + \delta r/2$ from the center of particle i, and $\delta N_i(r,\theta)$ is the particle number in a sector between $r - \delta r/2$ and $r + \delta r/2$ in the radial direction and $\theta - \delta\theta/2$ and $\theta + \delta\theta/2$ in the angular direction from the center of particle i; $\theta = 0$ and $\theta = \pi/2$ correspond to the spanwise and streamwise directions, respectively. In the present study, we set $\delta r = 0.08h$ ($\delta r^+ = 44$) and $\delta\theta = 0.025\pi$ to compute ADF(r,θ). The mean value is from the average of n_p particles from multiple snapshots in time. Finally, the distribution functions are normalized by the surface average particle number in the x-z plane ($n_p/L_x L_y$ representing a randomly distributed particle number density), where n_p particles are from the two-dimensional x-z slab taken in the wall-normal direction. Periodic boundary conditions are used for particles near the boundaries in the streamwise and spanwise directions.

ADF(r,θ) in the streamwise and spanwise directions corresponding to $\theta = \pi/2$ and $\theta = 0$ at two different wall-normal heights ($y^+ = 17$ and $y^+ = 300$) are shown in Fig. 9. For low-inertia

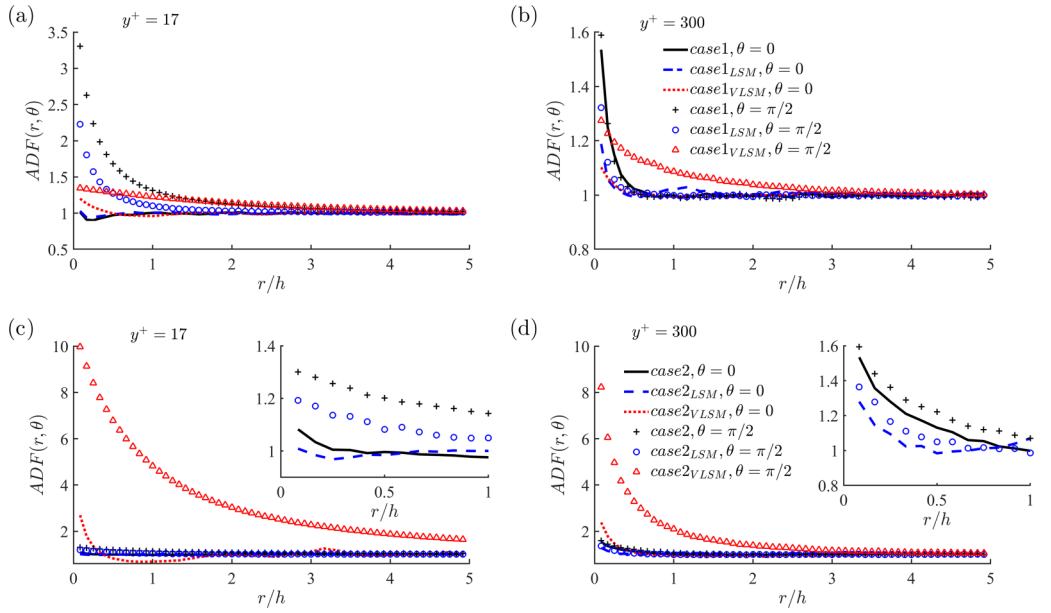

FIG. 9. The streamwise and spanwise angular distribution function (ADF) of particles in a slab with thickness of $2d_p$ at two wall-normal heights: near the wall [(a), (c)] at $y^+ = 17$; in the outer layer [(b), (d)] at $y^+ = 300$. For two Stokes numbers: [(a), (b)] low Stokes number; [(c), (d)] high Stokes number. The insets of panels (c) and (d) show enlargements of the region $r/h < 1$.

particles close to the wall, Fig. 9(a), the particle density from a reference particle in the streamwise direction is higher than in the spanwise direction, corresponding to the elongated anisotropic particle clustering formed in the inner layer as seen in Fig. 5(a). Compared with the full simulation, the difference in ADF between the streamwise and spanwise directions still exists in case1_{LSM}, whereas it diminishes for case1_{VLSM}. This indicates that the elongated anisotropic particle clustering is similar between case1_{LSM} and the full simulation [see also Figs. 5(c) and 5(a)], whereas the particle clustering tends to be more isotropic in case1_{VLSM} [Fig. 5(e)]. For low-Stokes-number particles in the outer region, as shown in Fig. 9(b), the ADF is similar between the streamwise and spanwise directions in both case1 and case1_{LSM}, corresponding to the quasi-isotropic particle clusters formed in the outer layer in Figs. 5(a) and 5(b). In case1_{VLSM}, we see that ADF in the streamwise direction remains larger than unity even at a distance of $2.5h$ from the reference particle, which indicates that there are streamwise elongated structures [observed in Fig. 5(b)], but not as pronounced as they are in the inner layer of case1.

The ADF of the high-Stokes-number particles is shown in Figs. 9(c) and 9(d). Compared with the full simulation, case2_{VLSM} shows a significant increase of the streamwise ADF and a sharp difference between the streamwise ADF and the spanwise ADF. The presence of this sharp difference in both Figs. 9(c) and 9(d) indicates that the elongated anisotropic particle clustering forms in both the inner layer and outer layer [see also Fig. 5(f)]. Meanwhile, comparing case2_{LSM} with the full simulation, ADF in the inner layer in both the streamwise and spanwise directions is slightly smaller than it is in case2 as shown in Fig. 9(c), while the difference is small in the outer layer as shown in Fig. 9(d).

The ADF profiles clearly show that the different particles respond in distinct ways to LSMs and VLSMs. As described above, the picture that develops is that low-inertia particles are influenced both by LSMs (which have a timescale more closely aligned with their own τ_p) and VLSMs. High-inertia particles, on the other hand, are more resistant to transport and accumulation triggered by LSMs, and instead are largely impacted by the dynamics of the VLSM structures. From the

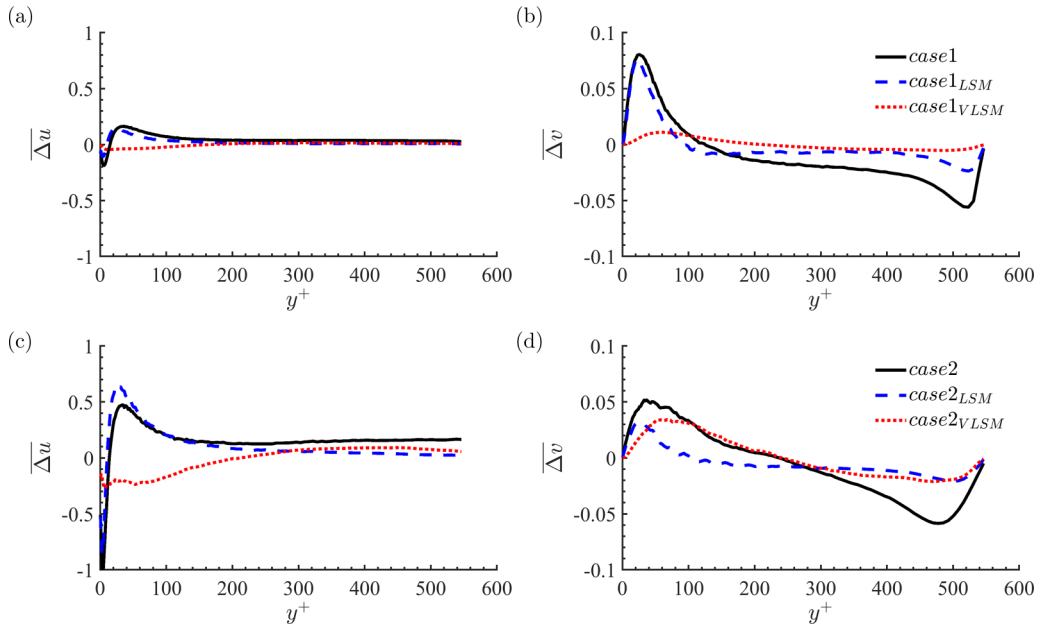

FIG. 10. Profiles of the slip velocity $\Delta u_i(y) = u_{f,i} - u_{p,i}$ normalized by u_τ. [(a), (c)] Streamwise velocity, $\overline{\Delta u}$; [(b), (d)] wall-normal velocity, $\overline{\Delta v}$. [(a), (b)] Low Stokes number; [(c), (d)] high Stokes number.

perspective of LES modeling, this would suggest (consistent with others [39,44]) that high-inertia particles simply coupled to the filtered velocity (i.e., which would fully resolve the VLSMs) may be able to predict the mean concentration and possibly even certain aspects of the particle spatial arrangement with sufficiently high accuracy. To better understand this difference between high- and low-inertia particles, the following section considers the slip velocity between the particle and filtered velocity fields.

3. Slip velocity

For particles with high inertia, a significant slip velocity ($\Delta u_i = u_{f,i} - u_{p,i}$) can exist, which describes the exchange of momentum between the fluid and particle phases. A good prediction of the slip velocities is essential to predicting particle trajectories in particle-laden LES [40], Reynolds-averaged Navier-Stokes (RANS) coupled laden with Lagrangian particles [66], or two-fluid modeling approaches [67]. Through the slip velocity, the drag force governs the particle trajectories and segregation [18], and subsequently modulates the turbulent flow [24,68,69].

In the inner layer of turbulent channel flow, Zhao *et al.* [70] find that in the streamwise direction the particles lead the fluid near the wall ($\overline{\Delta u} < 0$ in $y^+ < 20$), whereas the particles lag behind the fluid away from the wall ($\overline{\Delta u} > 0$ in $y^+ > 20$); the magnitude of the slip velocity increases monotonically with particle inertia. For the slip velocity in the wall-normal direction, particles lag behind the fluid near the wall ($\overline{\Delta v} > 0$ in $y^+ < 50$), whereas the particles lead the fluid away from the wall ($\overline{\Delta v} < 0$ in $y^+ > 50$) in Zhao *et al.* [70]. As shown in Fig. 10, we find a similar trend for both low- and high-inertia particles in the inner layer for the full simulations. In the outer layer ($y^+ > 100$), low-inertia particles tend to move toward the wall due to the negative mean drag force on the particle in the wall-normal direction. At the same time, the positive $\overline{\Delta v}$ near the wall indicates that low-inertia particles tend to move away from the wall in the range $y^+ < 100$. For high-inertia particles, the wall-normal slip velocity ($\overline{\Delta v}$) illustrates that high-inertia particles drift away from the wall not only in the inner layer but also for a portion of the outer layer ($100 < y^+ < 300$).

Generally, in the inner layer, low-inertia particles coupled only with LSMs (case1_{LSM}) produce the same sign and comparable magnitude of the slip velocity in the streamwise and wall-normal directions as shown in Figs. 10(a) and 10(b), respectively. However, high-inertia particles coupled with LSMs (case2_{LSM}) underpredict the $\overline{\Delta v}$ throughout most of the domain as shown in Fig. 10(d). In the outer layer, both of the filtering tests with either low- or high-inertia particles tend to underpredict the magnitude of the wall-normal slip velocity. This again seems to confirm that the slip velocity is primarily due to particles coupling with LSMs, especially in the streamwise direction and for low-inertia particles (case1_{LSM}), even while low-inertia particles can still be influenced in their bulk transport by VLSMs [cf. Figs. 6(a) and 6(b)]. This general conclusion is true even though the particle distribution itself would be modified if coupled to the full, unfiltered velocity field. High-inertia particles, on the other hand, coupled only with VLSMs (case2_{VLSM}) do not recover either slip velocity seen in the full simulation, even in the inner layer as shown in Fig. 10(d), so while the previous analysis of particle clustering and spatial arrangement would seem to suggest that high-inertia particles could simply be coupled to VLSMs (or the resolved scales of motion), this result indicates that if two-way coupling is an important feature, the slip velocity (and thus the two-way exchange of momentum between phases) is primarily determined by LSMs for *both* low- and high-inertia particles. This is particularly true in the streamwise direction [see Figs. 10(a) and 10(c)], whereas high-inertia particles coupled only with VLSMs do recover some of the wall-normal slip velocity near the wall [in Fig. 10(d)].

It therefore seems that for one-way particle dynamics, namely transport and spatial arrangement of inertial particles, it might be possible for high-inertia particles to be carried by large-scale motions (or resolved scales in the context of LES). Not surprisingly, low-inertia particles would require accurate subgrid treatment, or full resolution of the LSMs to capture their clustering and turbophoretic behavior. For two-way coupling, on the other hand, the high-inertia particles, while preferentially responding to the VLSMs, need information from the LSMs, since these dictate the mean slip velocity between the phases. In the final two sections, the consequences of this are demonstrated for the Reynolds stress and turbulent kinetic energy budgets in the context of two-way coupling.

4. Particle feedback to the Reynolds stress budget

The momentum exchange between the particle and fluid phases acts as a direct source-sink in the fluid Reynolds stress budgets. Particle sources to the $\overline{u'u'}$, $\overline{v'v'}$, and $\overline{u'v'}$ budget are denoted as $\overline{\Psi_{11}} = \overline{F_x'u'}$, $\overline{\Psi_{22}} = \overline{F_y'v'}$, and $\overline{\Psi_{12}} = \overline{F_x'v' + F_y'u'}$, respectively [56]. The particle sources are dependent on the characteristics of particle clusters [71] and also strongly related to the particle inertia [72]. Furthermore, Wang and Richter [23,24] demonstrate that both indirect and direct particle modulation mechanisms of LSMs and VLSMs have nonmonotonic relationships with particle inertia, which can be observed by the particles' modulation of the Reynolds stress budgets in spectral space.

Here we repeat a component of our previous analysis [23] and show the three particle source terms $\overline{\Psi_{11}}$ (to the $\overline{u'u'}$ budget), $\overline{\Psi_{22}}$ ($\overline{v'v'}$ budget), and $\overline{\Psi_{12}}$ ($\overline{u'v'}$ budget) in Fig. 11. In general, inertial particles coupled with LSMs (case1_{LSM} and case2_{LSM}) produce the same sign and comparable magnitude as the full simulations, whereas the particle sources are nearly zero for the case of inertial particles coupled with VLSMs (case1_{VLSM} and case2_{VLSM}). As suggested by the slip velocities presented in the previous section, this behavior of case1_{LSM} and case2_{LSM} shows that the particle sources to the Reynolds stress budgets are mainly dictated by the drag force interacting with small-scale structures (LSMs). This dominance of LSMs in the Reynolds stress budget is somewhat inconsistent to the direct enhancement mechanism of VLSMs by high-inertia particles (the enhancement of VLSMs energy related to $\overline{\Psi_{12}}$ at high wavelengths in the outer layer) observed by Wang and Richter [24], suggesting that the direct impact of high-inertia particles on VLSMs is weak compared to the nonlinear, indirect interaction through LSMs. In other words, the direct enhancement mechanism of VLSMs cannot be captured simply by artificial coupling between

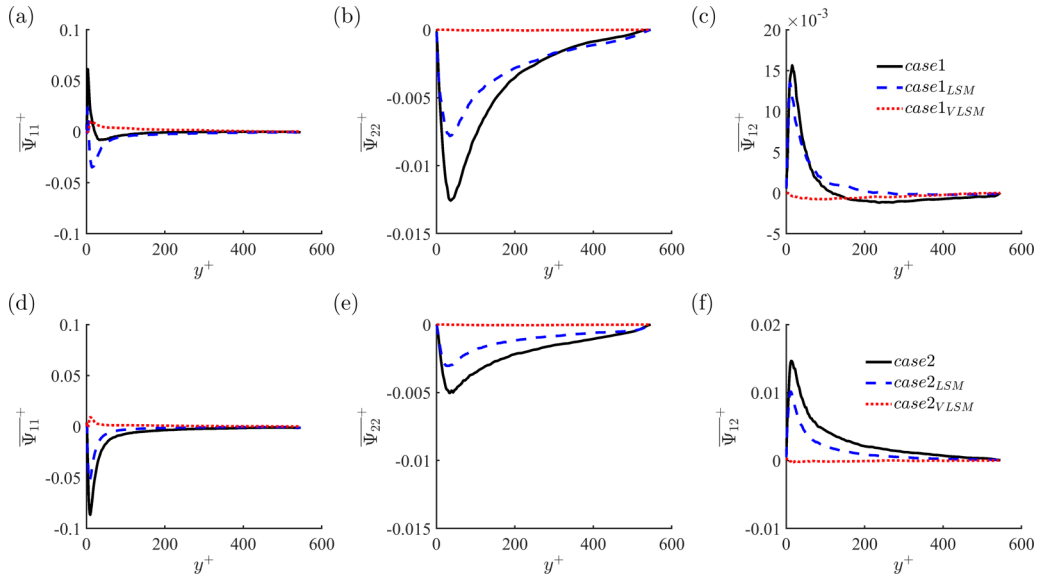

FIG. 11. Profiles of the particle feedback terms to Reynolds stress budget: [(a), (d)] particle sources to the $\overline{u'u'}$ budget, $\overline{\Psi_{11}}$; [(b), (e)] particle sources to the $\overline{v'v'}$ budget, $\overline{\Psi_{22}}$; [(c), (f)] particle sources to the $\overline{u'v'}$ budget, $\overline{\Psi_{12}}$. [(a)–(c)] Low Stokes number; [(d)–(f)] high Stokes number. All terms are scaled by u_τ^3/δ.

high-inertia particles and long-wavelength VLSM structures due to the underlying incorrect slip velocities in this case [seen in Figs. 10(c) and 10(d)]. It is clear that both turbulent structures (LSMs and VLSMs) work in tandem to simultaneously determine the correct particle dynamics, which further works on the local fluid to modulate the turbulence. Again, as stated previously, this mechanism poses a challenge for LES development of two-way coupled particle-laden flows: Even for high-inertia particles, it is LSMs which dictate momentum exchange. This upscale (in spectral space) influence, where both low- and high-inertia particles modify LSMs, which in turn can modulate VLSMs, is not a feature which could be captured by, say, an enhanced eddy diffusivity.

5. Interphasial energy transfer and particle dissipation

Due to the slip velocity induced by particle inertia, we have shown in Sec. III B 4 that the particles working on the fluid act as a direct source-sink in the Reynolds stress budgets. At the same time, the drag force working on the particles represents kinetic energy transferred from the fluid to the particles. The imbalance between the work transferred from the fluid to the particles compared to that from the particles to the fluid reflects energy dissipation, which may help describe the mechanism of drag reduction in particle-laden flow [69].

According to Zhao *et al.* [69], the time rate of the work done by the local fluid to a particle $\dot{W}_p$, the work done by a particle on the local fluid $\dot{W}_f$, and the dissipation to heat ϵ are expressed as

$$\dot{W}_p = 6\pi\mu a(u_{f,i} - u_{p,i})u_{p,i}, \tag{8}$$

$$\dot{W}_f = -6\pi\mu a(u_{f,i} - u_{p,i})u_{f,i}, \tag{9}$$

$$\epsilon = \dot{W}_p + \dot{W}_f = -6\pi\mu a(u_{f,i} - u_{p,i})(u_{f,i} - u_{p,i}), \tag{10}$$

where $u_{p,i}$ and $u_{f,i}$ are the particle velocity and the fluid velocity seen by the particle, respectively.

The quantities $\dot{W}_p$, $\dot{W}_f$, and ϵ are shown in Figs. 12(a) and 12(d), Figs. 12(b) and 12(e), and Figs. 12(c) and 12(f) for low- and high-Stokes-number particles, respectively. In the inner layer,

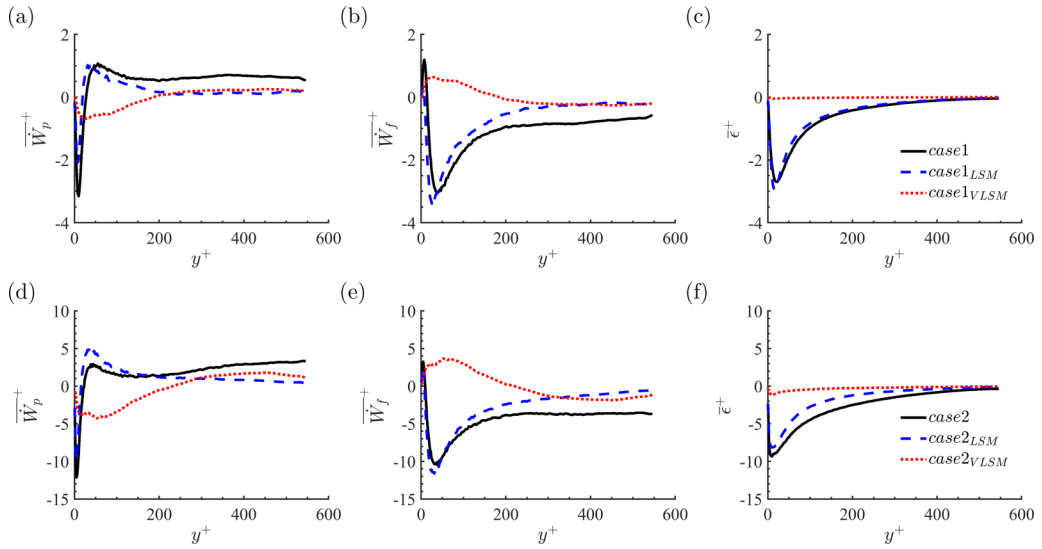

FIG. 12. Profiles of the mean power transferred between fluid and particles: [(a), (d)] from the fluid to the particle, $\overline{\dot{W}_p}$; [(b), (e)] from the particle to the fluid, $\overline{\dot{W}_f}$; [(c), (f)] the particle dissipation, $\overline{\epsilon}$. [(a)–(c)] Low Stokes number; [(d)–(f)] High Stokes number. The mean power is scaled by $6\pi\mu a u_\tau^2$.

the sign and trend of $\dot{W}_p$, $\dot{W}_f$, and ϵ profiles in full simulations (case1 and case2) are qualitatively similar to those obtained by Zhao *et al.* [69] in turbulent channel flow at $\mathrm{Re}_\tau = 180$. The respective responses to the various filtering methods are also qualitatively similar to the Reynolds stress budgets of Sec. III B 4.

The particles exert work on the local fluid in the buffer layer and viscous layer ($\overline{\dot{W}_p} < 0$, $\overline{\dot{W}_f} > 0$), whereas the particles receive energy from the fluid ($\overline{\dot{W}_p} > 0$, $\overline{\dot{W}_f} < 0$) beyond $y^+ = 40$. The energy transfer between the particles and the fluid is nearly the same between the particles coupled with LSMs (case1$_{LSM}$ and case2$_{LSM}$) and the full simulations (case1 and case2). However, as with the Reynolds stress budgets, large differences are seen between the VLSM coupling cases and the full simulations, not only in magnitude but also in sign. In the outer layer, both the low- and high-inertia particles continuously receive energy from the large-scale fluid motions ($\overline{\dot{W}_p} > 0$, $\overline{\dot{W}_f} < 0$), but the magnitude is smaller in both artificial coupling tests than it is in full simulation. As shown in Figs. 12(c) and 12(f), across the whole wall-normal height, the particle dissipation is comparable between particles coupled with LSMs and the full simulation, whereas $\overline{\epsilon}$ is negligible in both case1$_{VLSM}$ and case2$_{VLSM}$. This confirms that the particle dissipation generally comes from particles coupling with low-wavelength structures.

Consistent with the above discussions regarding the slip velocity (Fig. 10) and particle feedback to the Reynolds stress budget (Fig. 11), a similar conclusion can be drawn from the energy transfer characteristics: Two-way coupling is mainly a result of particle-LSM interaction, especially in the inner layer, and regardless of particle inertia. The strength of the two-way coupling is rather small in the case of only coupling with VLSMs in both the inner layer and outer layer. This again suggests that while VLSMs are important for distributing particles throughout the domain, and although their strength can be modulated by particles [24,72], it is fundamentally the coupling between LSMs and particles which dictates energy and momentum transfer between phases.

IV. CONCLUSION

In this study, we investigate the transport of inertial particles by large-scale motions (LSMs) and very-large-scale motions (VLSMs) in moderate-Reynolds-number ($\mathrm{Re}_\tau = 550$) open channel flow.

Two-particle Stokes numbers based on the characteristic timescales of the LSMs and VLSMs are used, where low-inertia particles with $\mathrm{St}_{LSM} = 0.3025$ preferably accumulate in LSMs in the inner layer [23] and high-inertia particles with $\mathrm{St}_{VLSM} = 0.331$ tend to form particle clustering structures associated with VLSMs in the outer layer [24]. While we focus only on two discrete Stokes numbers, an intriguing extension of this analysis is in the direction of polydispersed systems, where a broad spectrum of particle inertia would be interacting with a broad range of turbulent motions. Our results indicate that there would be multiple nonlinear interactions occurring simultaneously in this case, which lies outside the scope of the present effort.

The first test uses a truncated domain size to isolate VLSMs, since VLSMs can only be captured in a sufficiently large domain. By comparing the flow field between a small domain and large domain in single-phase flow, it is confirmed that the small domain can capture the correct length and intensity of LSMs in spectral space within the inner layer, even in the absence of VLSMs. As a consequence, an increase of up to 20% of the near-wall particle concentration is found in the large domain simulation as compared to the small domain. From a Voronoï tessellation analysis, particle clustering is stronger in the large domain simulation than it is in small domain simulation.

We then perform a series of artificial coupling tests, where through spatial filtering, the particles are only allowed to interact with certain features of the flow (i.e., thus isolating LSMs and VLSMs) in the large domain. The goal is to highlight the particle-flow interactions as a function of scale and inertia, to determine the range of motions which couple with particles of low and high Stokes numbers. Similar to the effect of truncating the domain size, the particle concentration and the underlying turbophoresis are underpredicted when VLSMs are absent. The particle clustering effect is more closely related to LSMs than VLSMs for both kinds of particles ($\mathrm{St}_{LSM} = 0.3025, 2.275$) as seen from Voronoï tessellation analysis. From a two-dimensional angular distribution function analysis, for low-inertia particles coupled only with VLSMs ($\mathrm{St}_{VLSM} = 0.044$), particle clustering is more isotropic than in full simulation in the inner layer, whereas weak, elongated streamwise anisotropic structures are formed in the outer layer. For high-inertia particles coupled with VLSMs ($\mathrm{St}_{VLSM} = 0.331$), strong, elongated streamwise anisotropic structures are formed in both the inner layer and the outer layer. Overall, low-inertia particle transport is dictated both by LSMs and VLSMs, while high-inertia particles are more influenced by VLSMs in the one-way coupled limit.

In the two-way coupled limit, however, analyses of the slip velocity, fluid Reynolds stress budget, and interphasial energy transfer highlight the importance of LSMs for both low- and high-inertia particles. The coupling between low-inertia particles and LSMs is anticipated, since the particle response time is chosen to match that of the LSMs. The high-inertia particles, by contrast, have a timescale associated with VLSMs, and yet their two-way coupling is dictated by their interactions with LSMs—i.e., coupling only with VLSMs provides very inaccurate exchanges of momentum and energy. This unfortunately does not mean that the effects of VLSMs can be ignored, however, since their energy content and contribution to the Reynolds stress can be altered by this small-scale two-way coupling (e.g., high-inertia particles strengthen the VLSMs due to direct interaction in the outer flow at high wavelengths through modulation of Reynolds stress budget [24]). It is also observed in this study that VLSMs are an integral part of the spatial distribution of particles. We emphasize here that care must be taken when interpreting the two-way coupled results, since our filtering strategy is not intended to perfectly separate certain interactions. When filtering is used on the velocity fields seen by the particles, the particles ultimately end up in different locations than they would have otherwise. Thus, quantities such as the slip velocity and energy transfer rates are a result of two simultaneous effects: inertial response of the particles as well as the difference in the particle distribution. Rather than concluding that this is precisely how inertial particles will interact with VLSMs or LSMs in full-spectrum turbulence, the goal is to inform efforts of understanding the consequences of cutoff filters on particle dynamics, such as those used in LES.

Thus, properly representing these effects remains an ongoing challenge in multiphase LES. In one-way coupled scenarios, particle-laden LES tends to underestimate turbophoresis with classic Lagrangian subgrid modes [37,39,73]. In this study, we find that although turbophoresis is induced by the presence of small-scale structures (i.e., LSMs), it will be underpredicted without considering

large-scale structures (i.e., VLSMs). These findings have implications on the development of subgrid models for particle one-way coupling in LES and on developing new Lagrangian subgrid models for the particle equation of motion which considers the effects of VLSMs. In the two-way coupled regime, the current study highlights the challenge of developing subgrid models which can properly capture the modulation of VLSMs [23], but through particle-LSM interactions which would not be resolved on an LES grid. Simply coupling low- or high-inertia particles to the resolved velocity field may not be sufficient in highly scale-separated, wall-bounded flows, and points to areas of future work ranging from ensuring that particle trajectories and distributions are faithfully replicated (i.e., in the one-way coupled sense) and that their two-way influence is felt appropriately at the resolved scales.

ACKNOWLEDGMENTS

The authors acknowledge Grants No. G00003613-ArmyW911NF-17-0366 from the U.S. Army Research Office and No. N00014-16-1-2472 from the U.S. Office of Naval Research. Computational resources were provided by the High Performance Computing Modernization Program (HPCMP) and by the Center for Research Computing (CRC) at the University of Notre Dame.

[1] K. Dyer and R. Soulsby, Sand transport on the continental shelf, Annu. Rev. Fluid. Mech. **20**, 295 (1988).
[2] J. F. Kok, E. J. Parteli, T. I. Michaels, and D. B. Karam, The physics of wind-blown sand and dust, Rep. Prog. Phys. **75**, 106901 (2012).
[3] F. Veron, Ocean spray, Annu. Rev. Fluid Mech. **47**, 507 (2015).
[4] A. Guha, Transport and deposition of particles in turbulent and laminar flow, Annu. Rev. Fluid. Mech. **40**, 311 (2008).
[5] R. A. Shaw, Particle-turbulence interactions in atmospheric clouds, Annu. Rev. Fluid Mech. **35**, 183 (2003).
[6] I. Nezu, Open-channel flow turbulence and its research prospect in the 21st century, J. Hydraul. Eng. **131**, 229 (2005).
[7] S. J. Kline, W. Reynolds, F. Schraub, and P. Runstadler, The structure of turbulent boundary layers, J. Fluid Mech. **30**, 741 (1967).
[8] J. Jiménez, Cascades in wall-bounded turbulence, Annu. Rev. Fluid. Mech. **44**, 27 (2011).
[9] K. C. Kim and R. J. Adrian, Very large-scale motion in the outer layer, Phys. Fluids **11**, 417 (1999).
[10] J. C. Del Álamo and J. Jiménez, Spectra of the very large anisotropic scales in turbulent channels, Phys. Fluids **15**, L41 (2003).
[11] N. Hutchins and I. Marusic, Evidence of very long meandering features in the logarithmic region of turbulent boundary layers, J. Fluid Mech. **579**, 1 (2007).
[12] B. Balakumar and R. Adrian, Large- and very-large-scale motions in channel and boundary-layer flows, Philos. Trans. R. Soc., A **365**, 665 (2007).
[13] M. Guala, S. Hommema, and R. Adrian, Large-scale and very-large-scale motions in turbulent pipe flow, J. Fluid Mech. **554**, 521 (2006).
[14] R. J. Adrian and I. Marusic, Coherent structures in flow over hydraulic engineering surfaces, J. Hydraul. Res. **50**, 451 (2012).
[15] J. R. Fessler, J. D. Kulick, and J. K. Eaton, Preferential concentration of heavy particles in a turbulent channel flow, Phys. Fluids **6**, 3742 (1994).
[16] Y. Pan and S. Banerjee, A numerical study of free-surface turbulence in channel flow, Phys. Fluids **7**, 1649 (1995).
[17] D. W. Rouson and J. K. Eaton, On the preferential concentration of solid particles in turbulent channel flow, J. Fluid Mech. **428**, 149 (2001).
[18] C. Marchioli and A. Soldati, Mechanisms for particle transfer and segregation in a turbulent boundary layer, J. Fluid Mech. **468**, 283 (2002).

[19] S. Balachandar and J. K. Eaton, Turbulent dispersed multiphase flow, Annu. Rev. Fluid. Mech. **42**, 111 (2010).
[20] G. Sardina, P. Schlatter, L. Brandt, F. Picano, and C. M. Casciola, Wall accumulation and spatial localization in particle-laden wall flows, J. Fluid Mech. **699**, 50 (2012).
[21] D. H. Richter and P. P. Sullivan, Momentum transfer in a turbulent, particle-laden Couette flow, Phys. Fluids **25**, 053304 (2013).
[22] J. Lee and C. Lee, Modification of particle-laden near-wall turbulence: Effect of Stokes number, Phys. Fluids **27**, 023303 (2015).
[23] G. Wang and D. Richter, Modulation of the turbulence regeneration cycle by inertial particles in planar Couette flow, J. Fluid Mech. **861**, 901 (2019).
[24] G. Wang and D. H. Richter, Two mechanisms of modulation of very-large-scale motions by inertial particles in open channel flow, J. Fluid Mech. **868**, 538 (2019).
[25] P. Gualtieri, F. Picano, G. Sardina, and C. M. Casciola, Clustering and turbulence modulation in particle-laden shear flows, J. Fluid Mech. **715**, 134 (2013).
[26] B. M. Sumer and R. Deigaard, Particle motions near the bottom in turbulent flow in an open channel. Part 2, J. Fluid Mech. **109**, 311 (1981).
[27] D. H. Richter and P. P. Sullivan, Modification of near-wall coherent structures by inertial particles, Phys. Fluids **26**, 103304 (2014).
[28] M. Caporaloni, F. Tampieri, F. Trombetti, and O. Vittori, Transfer of particles in nonisotropic air turbulence, J. Atmos. Sci. **32**, 565 (1975).
[29] M. Reeks, The transport of discrete particles in inhomogeneous turbulence, J. Aerosol Sci. **14**, 729 (1983).
[30] M. Bernardini, S. Pirozzoli, and P. Orlandi, The effect of large-scale turbulent structures on particle dispersion in wall-bounded flows, Int. J. Multiphase Flow **51**, 55 (2013).
[31] S. Pirozzoli, M. Bernardini, and P. Orlandi, Large-scale motions and inner/outer layer interactions in turbulent Couette-Poiseuille flows, J. Fluid Mech. **680**, 534 (2011).
[32] T. Tsukahara, H. Kawamura, and K. Shingai, DNS of turbulent Couette flow with emphasis on the large-scale structure in the core region, J. Turbulence **7**, 1 (2006).
[33] V. Avsarkisov, S. Hoyas, M. Oberlack, and J. García-Galache, Turbulent plane Couette flow at moderately high Reynolds number, J. Fluid Mech. **751**, R1 (2014).
[34] D. V. Papavassiliou and T. J. Hanratty, Interpretation of large-scale structures observed in a turbulent plane Couette flow, Int. J. Heat Fluid Flow **18**, 55 (1997).
[35] S. Toh and T. Itano, Interaction between a large-scale structure and near-wall structures in channel flow, J. Fluid Mech. **524**, 249 (2005).
[36] G. Wang, H. J. Park, and D. Richter, Effect of computational domain size on inertial particle one-point statistics in open channel flow, Int. J. Multiphase Flow **125**, 103195 (2020).
[37] J. G. Kuerten, Point-particle DNS and LES of particle-laden turbulent flow-a state-of-the-art review, Flow, Turbul. Combust. **97**, 689 (2016).
[38] Q. Wang and K. D. Squires, Large eddy simulation of particle-laden turbulent channel flow, Phys. Fluids **8**, 1207 (1996).
[39] C. Marchioli, M. V. Salvetti, and A. Soldati, Some issues concerning large-eddy simulation of inertial particle dispersion in turbulent bounded flows, Phys. Fluids **20**, 040603 (2008).
[40] P. Fede and O. Simonin, Numerical study of the subgrid fluid turbulence effects on the statistics of heavy colliding particles, Phys. Fluids **18**, 045103 (2006).
[41] G. Jin, G.-W. He, L.-P. Wang, and J. Zhang, Subgrid scale fluid velocity timescales seen by inertial particles in large-eddy simulation of particle-laden turbulence, Int. J. Multiphase Flow **36**, 432 (2010).
[42] E. Pitton, C. Marchioli, V. Lavezzo, A. Soldati, and F. Toschi, Anisotropy in pair dispersion of inertial particles in turbulent channel flow, Phys. Fluids **24**, 073305 (2012).
[43] A. J. Smits, B. J. McKeon, and I. Marusic, High-Reynolds number wall turbulence, Annu. Rev. Fluid Mech. **43**, 353 (2011).
[44] Y. Yamamoto, M. Potthoff, T. Tanaka, T. Kajishima, and Y. Tsuji, Large-eddy simulation of turbulent gas-particle flow in a vertical channel: Effect of considering inter-particle collisions, J. Fluid Mech. **442**, 303 (2001).

[45] G. I. Park, M. Bassenne, J. Urzay, and P. Moin, A simple dynamic subgrid-scale model for LES of particle-laden turbulence, Phys. Rev. Fluids **2**, 044301 (2017).
[46] L. Schiller and A. Z. Naumann, Über die grundlegenden Berechnungen bei der Schwerkraftaufbereitung, Z. Ver. Dtsch. Ing. **77**, 318 (1933).
[47] M. R. Maxey and J. J. Riley, Equation of motion for a small rigid sphere in a nonuniform flow, Phys. Fluids **26**, 883 (1983).
[48] J. Capecelatro and O. Desjardins, An Euler-Lagrange strategy for simulating particle-laden flows, J. Comput. Phys. **238**, 1 (2013).
[49] G. Sardina, K. Jareteg, H. Ström, and S. Sasic, Assessing the ability of the Eulerian-Eulerian and the Eulerian-Lagrangian frameworks to capture meso-scale dynamics in bubbly flows, Chem. Eng. Sci. **201**, 58 (2019).
[50] P. Gualtieri, F. Picano, G. Sardina, and C. M. Casciola, Exact regularized point particle method for multiphase flows in the two-way coupling regime, J. Fluid Mech. **773**, 520 (2015).
[51] G. Akiki, W. Moore, and S. Balachandar, Pairwise-interaction extended point-particle model for particle-laden flows, J. Comput. Phys. **351**, 329 (2017).
[52] G. Wang, K. O. Fong, F. Coletti, J. Capecelatro, and D. Richter, Inertial particle velocity and distribution in vertical turbulent channel flow: a numerical and experimental comparison, Int. J. Multiphase Flow **120**, 103105 (2019).
[53] K. O. Fong, O. Amili, and F. Coletti, Velocity and spatial distribution of inertial particles in a turbulent channel flow, J. Fluid Mech. **872**, 367 (2019).
[54] Y. Pan and S. Banerjee, Numerical simulation of particle interactions with wall turbulence, Phys. Fluids **8**, 2733 (1996).
[55] Y. Yamamoto, T. Kunugi, and A. Serizawa, Turbulence statistics and scalar transport in an open-channel flow, J. Turbul. **2**, 1 (2001).
[56] G. Wang, M. Abbas, and E. Climent, Modulation of large-scale structures by neutrally buoyant and inertial finite-size particles in turbulent Couette flow, Phys. Rev. Fluids **2**, 084302 (2017).
[57] O. Flores and J. Jiménez, Hierarchy of minimal flow units in the logarithmic layer, Phys. Fluids **22**, 071704 (2010).
[58] Y. Hwang and C. Cossu, Self-Sustained Process at Large Scales in Turbulent Channel Flow, Phys. Rev. Lett. **105**, 044505 (2010).
[59] A. Lozano-Durán and J. Jiménez, Effect of the computational domain on direct simulations of turbulent channels up to $\mathrm{Re}_\tau = 4200$, Phys. Fluids **26**, 011702 (2014).
[60] J. Jiménez and P. Moin, The minimal flow unit in near-wall turbulence, J. Fluid Mech. **225**, 213 (1991).
[61] J. Jiménez, J. C. Del Alamo, and O. Flores, The large-scale dynamics of near-wall turbulence, J. Fluid Mech. **505**, 179 (2004).
[62] J. M. Hamilton, J. Kim, and F. Waleffe, Regeneration mechanisms of near-wall turbulence structures, J. Fluid Mech. **287**, 317 (1995).
[63] H. Abe, H. Kawamura, and H. Choi, Very large-scale structures and their effects on the wall shear-stress fluctuations in a turbulent channel flow up to $\mathrm{Re}_\tau = 640$, J. Fluids Eng. **126**, 835 (2004).
[64] R. Monchaux, M. Bourgoin, and A. Cartellier, Preferential concentration of heavy particles: a Voronoï analysis, Phys. Fluids **22**, 103304 (2010).
[65] R. Monchaux, M. Bourgoin, and A. Cartellier, Analyzing preferential concentration and clustering of inertial particles in turbulence, Int. J. Multiphase Flow **40**, 1 (2012).
[66] B. Arcen and A. Tanière, Simulation of a particle-laden turbulent channel flow using an improved stochastic lagrangian model, Phys. Fluids **21**, 043303 (2009).
[67] O. Simonin, E. Deutsch, and J. Minier, Eulerian prediction of the fluid/particle correlated motion in turbulent two-phase flows, Appl. Sci. Res. **51**, 275 (1993).
[68] T. Tanaka and J. K. Eaton, Classification of Turbulence Modification by Dispersed Spheres Using a Novel Dimensionless Number, Phys. Rev. Lett. **101**, 114502 (2008).
[69] L. Zhao, H. I. Andersson, and J. J. Gillissen, Interphasial energy transfer and particle dissipation in particle-laden wall turbulence, J. Fluid Mech. **715**, 32 (2013).

[70] L. Zhao, C. Marchioli, and H. Andersson, Stokes number effects on particle slip velocity in wall-bounded turbulence and implications for dispersion models, Phys. Fluids **24**, 021705 (2012).

[71] J. Capecelatro, O. Desjardins, and R. O. Fox, On the transition between turbulence regimes in particle-laden channel flows, J. Fluid Mech. **845**, 499 (2018).

[72] D. H. Richter, Turbulence modification by inertial particles and its influence on the spectral energy budget in planar Couette flow, Phys. Fluids **27**, 063304 (2015).

[73] B. Vreman, B. J. Geurts, N. Deen, J. Kuipers, and J. G. Kuerten, Two- and four-way coupled Euler-Lagrangian large-eddy simulation of turbulent particle-laden channel flow, Flow, Turbul. Combust. **82**, 47 (2009).